Nanoscale

COMMUNICATION

View Article Online
View Journal | View Issue

Cite this: *Nanoscale*, 2019, **11**, 3129

Received 28th September 2018,
Accepted 20th January 2019

DOI: 10.1039/c8nr07912a

rsc.li/nanoscale

High-performance field emission based on nanostructured tin selenide for nanoscale vacuum transistors†

Huu Duy Nguyen, Joon Sang Kang, Man Li and Yongjie Hu *

Vacuum field effect transistors have been envisioned to hold the promise of replacing solid-state electronics when the ballistic transport of electrons in a nanoscale vacuum can enable significantly high switching speed and stability. However, it remains challenging to obtain high-performance and reliable field-emitter materials. In this work, we report a systematic study on the field emission of novel two-dimensional tin selenide (SnSe) with rational design of its structures and surface morphologies. SnSe in the form of atomically smooth single crystals and nanostructures (nanoflowers) is chemically synthesized and studied as field emitters with varying channel lengths from 6 μm to 100 nm. Our study shows that devices based on SnSe nanoflowers significantly improve the performance and enable field emission at a reduced voltage due to a surface-enhanced local electrostatic field, and further lead to nonlinear dependent channel scaling when the channel length is shorter than 600 nm. We measured a record-high short-channel field-enhancement factor of 50 600 for a 100 nm device. Moreover, we investigated the emission stability and measured the fluctuations of the emission current which are smaller than 5% for more than 20 hours. Our results demonstrated a high-performance and highly reliable field emitter based on 2D SnSe nanostructures and we developed an important building block for nanoscale vacuum field effect transistors.

Solid-state electronics has powered the information technology revolution since the 1960s; however, its continuous scaling following Moore's law is nearing the end due to many intrinsic challenges.[1–10] Beyond the traditional metal–oxide–semiconductor field-effect transistors (MOSFETs), advanced design based on new materials and device operation are needed to further improve the speed and performance. Novel 1D and 2D nanomaterials have been the research focus over the last few decades and enabled new opportunities. Nanowires,[11–15] carbon nanotubes,[16–19] and graphene transistors[20,21] have been intensively studied. In particular, a Ge/Si nanowire heterostructure has been created and enabled high-performance transistors to significantly outperform silicon MOSFETs with a 2 THz intrinsic switching speed with a 40 nm channel length device.[11–15] Other efforts include improving the gate coupling and reducing short-channel effects such as using the surrounding gate and FinFETs[22–24] as well as developing new operation paradigms such as tunneling transistors,[25] piezoelectronic transistors,[26] ferroelectric-gate FETs,[27] spintronics,[13,14,28] and memristors and neuromorphic devices.[29,30] These proposed new devices aimed at circumventing the intrinsic limitations of MOSFETs and at lowering the transistor's power consumption.

Despite the traditional focus on solid-state electronics, the transport of electrons in a vacuum in principle allows for orders of higher velocities than that in the solid state. The high-speed operation is also expected at atmospheric pressure under a small anode–cathode gap below the electron mean free paths in air, which leads to a sufficiently low scattering probability between the electrons and gas molecules. For this motivation, more recently, vacuum field effect transistors (VFETs) have been proposed as an attractive concept beyond solid-state devices. VFETs use vacuum as their channel instead of the traditional doped silicon channel for charge carrier transport; the electrons travel across the vacuum channel *via* ballistic field emission to enable high speed. Due to this, VFETs are also expected to have high temperature and radiation tolerance, and their operating frequency is expected to be at least ten times higher than that of the traditional MOSFETs.[31–33] In addition, by reducing the channel length below the mean free path of electrons in air (~100 nm), VFETs can be operational in air due to the low probability of collision of electrons and air molecules;[31] this effectively removes the high vacuum requirement of VFETs. However, experimental efforts on VFETs have been scarce. Silicon-based devices are among those that were first explored for VFETs due to the ease of fabrication.[34–38] These early studies show good promise in

School of Engineering and Applied Science, University of California, Los Angeles, Los Angeles, CA, 90095, USA. E-mail: yhu@seas.ucla.edu

†Electronic supplementary information (ESI) available. See DOI: 10.1039/c8nr07912a

building nanoscale vacuum devices but also indicate the need for material improvement. In particular, the instability and the high turn-on voltage of emitter materials present a major challenge. On the other hand, recent literature efforts in studying new materials for field emission provide useful insights. Diamond is one of the most popular materials for field emission application due to its low work function and negative electron affinity, but diamond suffers from high cost, slow growth rates, low quality, and challenging processing with semiconductors. Carbon nanotubes, nanowires, and two-dimensional materials such as graphene have been studied because of their high aspect ratio and unique nanoscale geometry for field emission.[39–53] However, for VFET application, a low turn-on voltage and high stability in air are yet to be demonstrated.

Fundamentally, several merits are needed for the ideal VFET emitter material: first, a low work function is desired for low electron tunneling barrier, thereby introducing a small turn-on voltage. Second, materials with high atomic bond energy are desirable to maintain long-term stable field emission and prevent degradation.[39] For these required properties, tin selenide (SnSe) seems to be a good candidate for VFETs. SnSe is a 2D material with an orthorhombic crystal structure, naturally providing nanoscale field emission tipping down to a single atomic layer. The bonding energy of SnSe is ~4.16 eV,[54] higher than those of other materials: 3.21 eV for silicon,[54] 2.59 eV for ZnO,[54] and 2.56 eV for MoS_2.[55] The work function of SnSe (3.9 eV)[56] is also low, considering most studied materials. SnSe has been recently studied for thermoelectric applications due to its record-high figure of merit.[57,58] However, its field emission properties have not been explored so far. Here, we investigated for the first time the field emission performance and stability of SnSe with controlled nanostructure morphologies.

To evaluate the effect of surface morphologies on the field emission performance, we used two different chemical synthesis approaches to control the structures of SnSe in the shape of regular crystals and nanoflowers. First, SnSe single crystals (SCs) with an atomically flat crystalline plane surface are prepared *via* the vapor transport method to make large SnSe crystals (see the ESI†). Sn and Se atoms are covalently bound with a bond length of ~3.1 Å along the in-plane direction and ~2.75 Å along the cross-plane direction,[59] and the layers are weakly bound together by van der Waals force (Fig. 1a). The as-synthesized SC is large but rough (inset of Fig. 1b), which is not suitable for our experiment; therefore, we mechanically exfoliated the crystal to make a flat surface. The SEM image of the exfoliated SC (Fig. 1b) reveals the large smooth surface with a few broken edges along the in-plane direction of the SnSe crystal. Second, the SnSe nanostructure in the structure of flowers, *i.e.* nanoflowers (NFs), is synthesized using the solution reaction method based on ref. 60

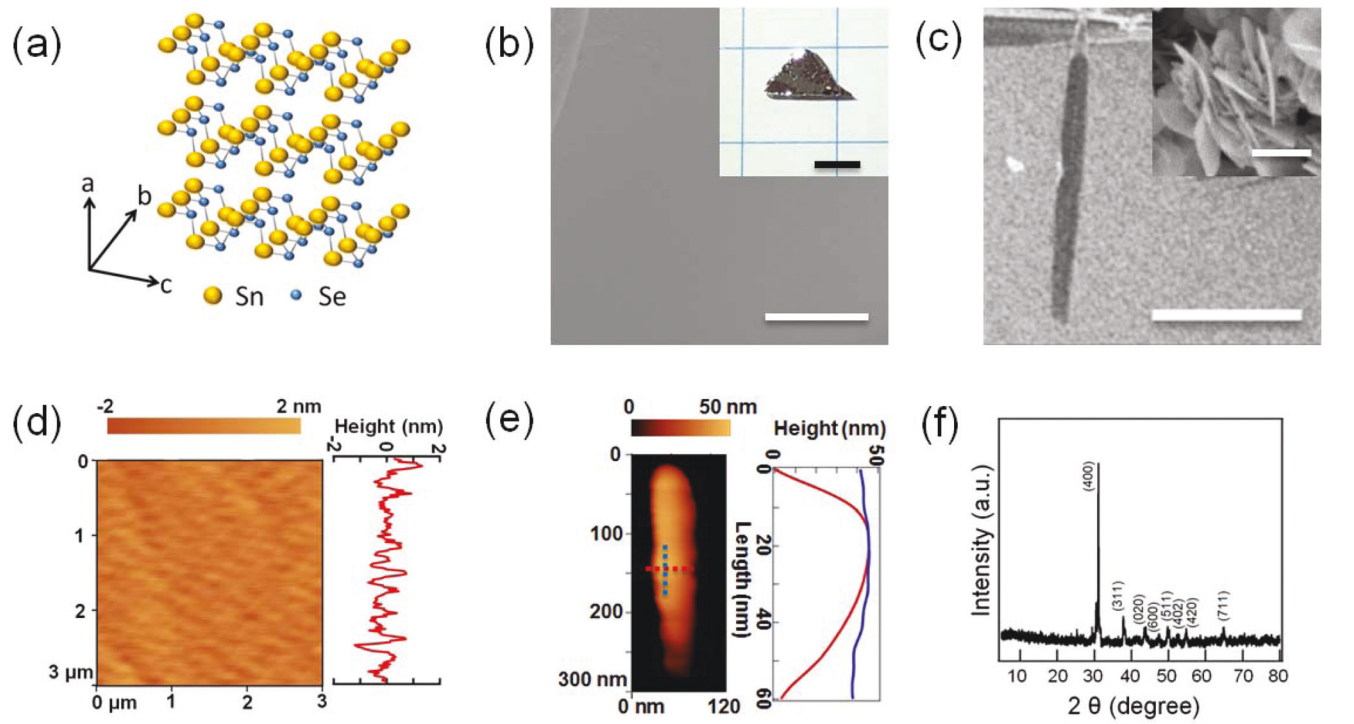

Fig. 1 Structural design and characterization of tin selenide (SnSe). (a) Schematic illustration of the 2D crystal structure of SnSe. (b) Scanning electron microscopy image (SEM) of an exfoliated SnSe single-crystal (SC) sample; the scale bar is 50 μm. The inset is an optical image of an as-synthesized crystal; the scale bar is 3 mm. (c) SEM image of a single tip of the SnSe nanoflower (NF); the scale bar is 10 μm. The inset is the NF arrays; the scale bar is 500 nm. (d) Atomic force microscopy (AFM) image of the SnSe SC sample. The inset is a one-dimensional surface scan extracted from the AFM image. (e) AFM image along a tip of the SnSe NF. On the right side is the one-dimensional surface profile of the tip, with the red and blue profiles corresponding to the dashed red and blue lines in the AFM image. (f) Powder X-ray diffraction of SnSe.

(see the ESI†). In Fig. 1c, a single piece of the NF has been examined by SEM, which clearly shows that a nanoscale sharp tip could enhance the electric field, while the whole sample on a cm scale (inset, Fig. 1c) reveals a dense flower-like morphology[60] that largely increases the surface areas for high power emission with a high current density. From the SEM image, we estimate that the average diameter of a NF particle is around 1.2 μm and the sharp tip is 20–60 nm thick in the cross-plane direction and 300–500 nm long in the in-plane direction. Moreover, the SEM images showed that the tip of the NF is similar to a cylindrical nanowire that enhances field emission. Such a large aspect ratio between the thickness of the tip and the size of the NF indicates that the NF-based emitter would strongly improve emission efficiency. We further use atomic force microscopy (AFM) to characterize the exact surface profile of both the SC and NF in order to calculate the field enhancement factor. The AFM image of the exfoliated SC revealed a flat surface with roughness below 2 nm (Fig. 1d). The AFM data also show that the surface profile of a NF tip is a plane-like structure, forming an emission tip of about 60 nm thick and 300 nm long (Fig. 1e). Finally, we use powder X-ray diffraction (XRD) to characterize the crystal lattice structure of our samples. Fig. 1f shows that the sharp peaks we observed are corresponding to orthorhombic SnSe with the *Pnma* space group #62 (ICDD #00-014-0159) with lattice constants of 11.5 Å, 4.1 Å, and 4.4 Å in *a*, *b*, and *c* directions, respectively. In addition, the sharp peaks shown in Fig. 1f indicate the good crystallinity of our samples.

Next, to investigate the field emission performance of SnSe, we fabricate field emission devices using the two different SnSe samples as the emitters. The field emission measurement of SnSe is configured in diode configurations as shown in Fig. 2a. We use an oxide insulation layer to control the channel length with SnSe as a cathode emitter and gold-coated glass as an anode. To make a comparison, we fabricate field emitters based on a single piece of the SnSe SC and SnSe NF. The SnSe SC cathode was made by exfoliating the crystal to create an atomic smooth surface (top of Fig. 2a). The SnSe NF cathode was fabricated using ebeam lithography and atomic layer deposition (bottom of Fig. 2a). A gold film was used as the anode for both devices and was deposited by e-beam evaporation. The channel distance was designed using a thin film of aluminum oxide deposited onto the substrate prepared from ebeam evaporation (middle of Fig. 2a). This fabrication method effectively creates an 80 μm wide channel with its length controlled by the oxide's thickness. A single field emission device is formed between the gold film and a SnSe SC/NF tip, and its channel length is verified by SEM. As examples shown in Fig. 2b and c, the channel length between SnSe and the anode is ~100 nm, which is taken as the distance between

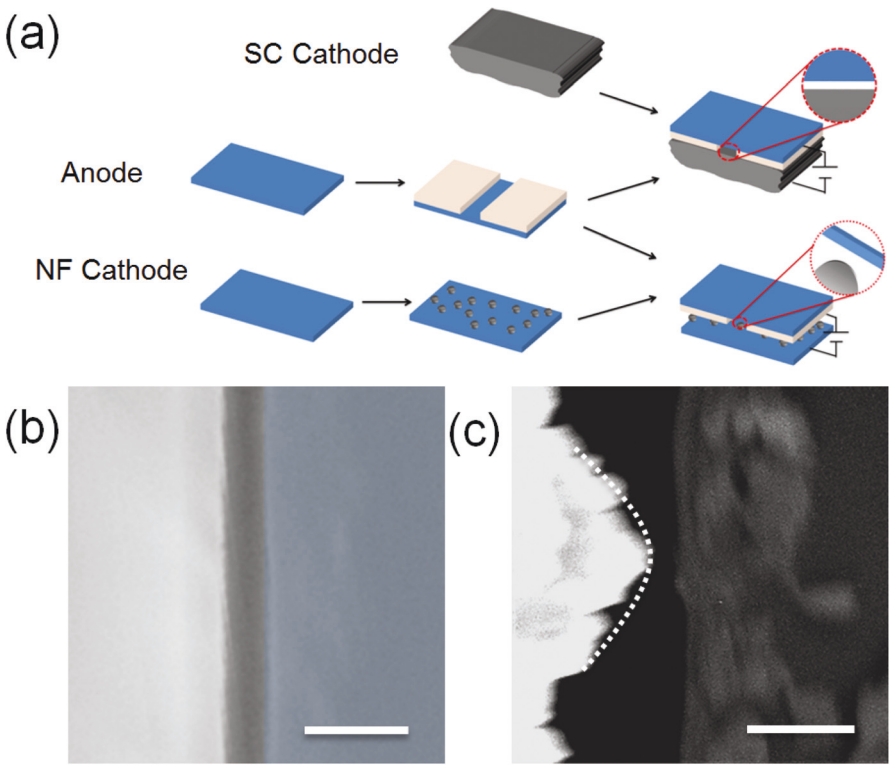

Fig. 2 Fabrication of SnSe field emission devices. (a) Schematic of the fabrication process. The SnSe emitter, metal collector, and oxide insulation layer are illustrated, respectively, in black, blue, and light pink colors. The fabrication steps are illustrated using the SnSe single crystal (SC) as the emitter (top), gold as the collector (middle), and the SnSe nanoflower (NF) as the emitter (bottom). (b) SEM image of a SnSe SC device with a 100 nm channel. The false color is used to highlight the SnSe SC (white) and the anode (blue). Scale bar, 250 nm. (c) SEM image of a SnSe NF device with a 100 nm channel. The dashed curve illustrates the parabolic profile of a single NF tip. Scale bar, 500 nm.

the two flat surfaces (for the SC case) and between the apex of the tip of the NF and the flat anode. The SEM images reveal the smooth surface of the SC, while the tip of the NF is a very sharp parabolic tip with many protrusions.

Next, careful electrical transport measurements were formed on the fabricated devices to evaluate their field emission performance in comparison with other materials and to determine how the surface morphology of the SC and NF alters the field emission. The samples were measured in air at room temperature and ambient pressure. To initiate field emission, we slowly increase the bias DC voltage between the cathode and anode at 0.01 V per increment and record the emission current. The measured field emission *J–V* curves for SC and NF devices with a 100 nm channel are plotted in Fig. 3a. The field emission curve is similar to that of a diode device as shown in Fig. 3a: the measured current density is small until the bias voltage reaches a turn-on voltage, then it begins to exponentially increase. This originates from vacuum tunneling which requires that the electrons have enough energy at high bias voltage to tunnel across the vacuum barrier *via* field emission. In general, the field emission was modeled by the Fowler–Nordheim (FN) equation given as

$$I = A\frac{aV^2\beta^2}{h^2\varphi}\exp\left(-\frac{b\varphi^{1.5}h}{V\beta}\right) \quad (1)$$

where A is the emitter's effective area, h is the vacuum channel length between the anode and the SnSe cathode emitter through which the electron tunnels, φ is the emitter's work function, β is the field enhancement factor, which is defined as the ratio of the local electric field around the emitter to the macroscopic applied electric field, and a and b are constants with $a = 1.54 \times 10^{-6}$ A eV V^{-2} and $b = 6.83 \times 10^{9}$ eV$^{-1.5}$ V m^{-1}. From eqn (1), it can be seen that the field emission current is largely influenced by the work function, field enhancement factor, and channel length. Therefore, a small work function and channel length and a large field enhancement factor are needed to achieve a large emission current with a low turn-on voltage. The SnSe NF in Fig. 3a has a higher emission current density in comparison with the SC, which is attributed to the parabolic profile of the NF tip, where the local electric field is strongly enhanced *versus* a flat surface. The turn-on voltage is extracted through the linear extrapolation of the *J–V* curve. From Fig. 3a, the turn-on voltage of the 100 nm channel NF device is 0.4 V, which is significantly lower than that in the literature;[34,35] we attribute this to the small channel length and the low work function of SnSe.

We replot our emission curve in the FN plot ($\log(I/V^2)$ *vs.* $1/V$) in Fig. 3b; the prediction lines using the FN equation are plotted for comparison, which verifies that field emission is the dominant electron transport mechanism. In Fig. 3b, the NF yields two straight lines, which indicate two different emission regions; similarly, the FN plot for the SC also yields two straight lines (inset of Fig. 3b). To further evaluate the field emission performance, we extract the key performance metrics of field emission devices, more specifically the field enhancement factor. The field enhancement factor from the slopes of linear regions is evaluated by assuming that the channel length h varies with the emitter's morphology, so the FN equation is rewritten as

$$I = \int\int \frac{aV^2\beta^2}{h(x,y)^2\varphi}\exp\left(-\frac{b\varphi^{1.5}h(x,y)}{V\beta}\right)\mathrm{d}x\mathrm{d}y \quad (2)$$

and the slope of the straight line in the FN plot is then calculated as

$$\frac{d\left(\ln\left(\frac{I}{V^2}\right)\right)}{d\frac{1}{V}} = \frac{d\ln\left(\int\int \frac{\beta^2}{h(x,y)^2}\exp\left(-\frac{b\varphi^{1.5}h(x,y)}{V\beta}\right)\mathrm{d}x\mathrm{d}y\right)}{d\frac{1}{V}}. \quad (3)$$

Assuming that only a single petal tip emits electrons (with an area of ~60 nm × 300 nm from Fig. 1e) for the NF and an arbitrary area for the flat surface, by matching the experimental data in Fig. 3b and the morphology of the NF tip and the SC flat surface, the field enhancement factors of the SC are 320 and 76 for the first and second regions, respectively, and the field enhancement factors of the NF are 50 600 and 7930 for the first and second regions (see the ESI†). Interestingly, the field enhancement factor of 50 600 measured in the NF

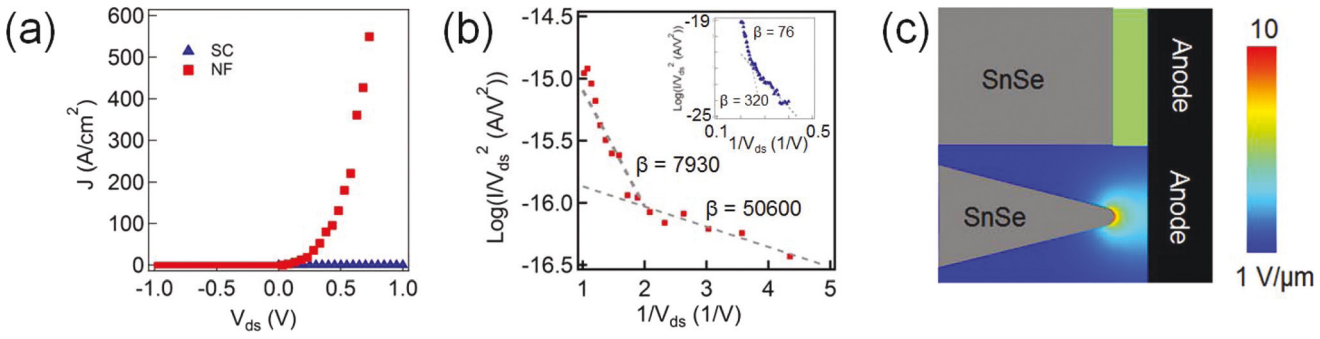

Fig. 3 Field emission measurement of 100 nm channel SnSe devices. (a) *J–V* curves of 100 nm channel devices using the SnSe SC (blue) and the NF (red) as the emitter. (b) The Fowler–Nordheim (FN) plot of the NF showed two emission regions. Inset is the FN plot of the SC. The dashed line represents a linear fit of the emission regions. (c) The electrostatic field simulated with COMSOL for the SC (top) and a tip of the NF (bottom).

emitter is record high compared to the reported literature with a similar channel length.[61] The field enhancement factor of the SnSe NF is much larger than that of the SC as expected due to its morphology. However, the first region of the SC has an unusually large field enhancement factor, considering that the emitter is a flat surface; the second region has a lower field enhancement factor and is more realistic. This phenomenon has been observed over the past few decades for other emitters;[33,34,62] the first emission region most likely originates from the surface roughness we observed in our AFM and SEM measurements (Fig. 1b and d) and the second region originates from the combination of the whole flat surface of the SC and the roughness. Likewise, the first emission region of the NF with a record high field enhancement factor of 50 600 is due to the protrusions that we observed in Fig. 2c, while the second emission region originates from both protrusions and the NF tip. For 100 nm devices, the ratio of field enhancement factors between the NF and SC is about 158 and 104, respectively, for the two emission regions, indicating that the field enhancement contribution from the surface morphology of the NF is about 100 times dominant over that from the channel distances.

The extracted high field enhancement factor is attributed to the unique nanostructures and field emission geometry of the SnSe devices. On the other hand, we note that there are physical and mathematical assumptions for typical FN-type equations, *i.e.* the orthodox emission hypothesis.[63] In particular, (i) the emitting surface is treated as uniform voltage; (ii) the measured emission current is equal to the device current; (iii) emission is treated as deep tunneling through a Schottky–Nordheim barrier with quantities independent of the voltage; and (iv) the local work function of the emitter is constant. Additional factors may break these hypotheses and introduce deviations from the orthodox emission hypothesis. For example: the voltage non-uniformity in the emitting regions and surrounding counter-electrodes for non-metal emitters can likely break condition (i); possible scattering or leakage that introduces inequality between the emission current and the measured device current may break condition (ii); dependent variables and barrier-form correction factors in the FN-type equation can break condition (iii); and local surface trapped charge or defects can result in a non-uniform work function of the emitter surface and break condition (iv). Scaling down the tunneling channel or emitter size may make it even hard to satisfy such orthodox emission hypothesis due to more stringent geometric requirements at the nanoscale. Therefore, a more sophisticated data-analysis theory can help better understand the field emission mechanisms for novel materials and nanoscale field emission geometries.

To further study the origin of field emission, we use finite-element methods to simulate the electric field in SC and NF devices (Fig. 3c). We model the SC as a 1 mm thick substrate with a flat surface expose to the anode (top of Fig. 3c); for simplicity, the NF tip is modeled as a 1.2 μm rod with a round tip of 60 nm diameter (bottom of Fig. 3c). We set the gap between

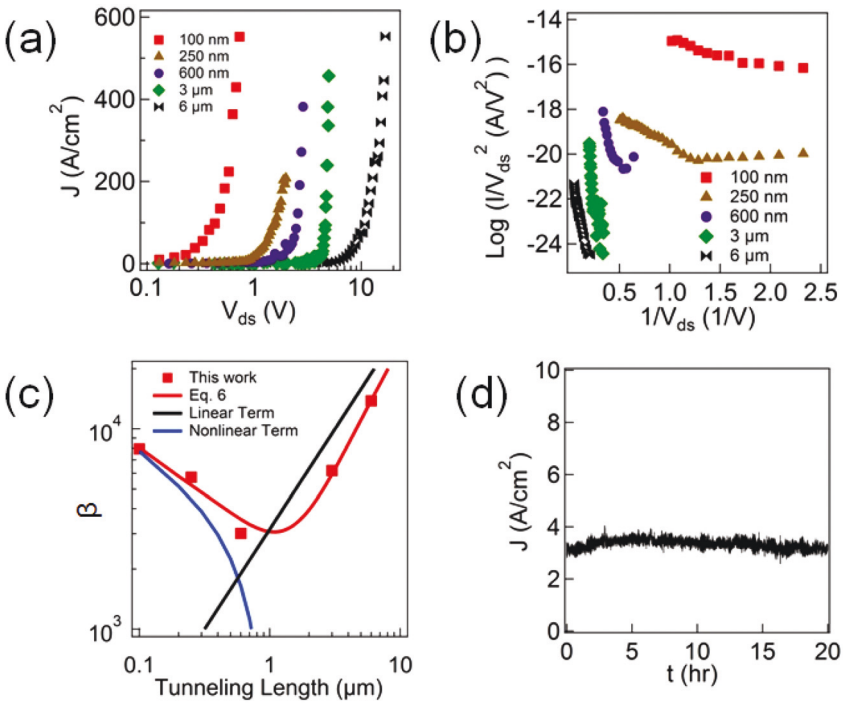

Fig. 4 Field emission measurement of SnSe nanoflower (NF) devices with channel length scaling. (a) Field emission *J*–*V* data of SnSe NF devices with a channel with length from 6 μm to 100 nm. (b) The Fowler–Nordheim plot of the measured field emission of SnSe NF devices with different channel lengths. (c) Field enhancement factor (β) from the measurement (red dot) and empirical fitting (red line) as a function of the channel length. The contribution of linear and non-linear terms in eqn (6) are plotted in black and blue lines, respectively. (d) Emission stability over 20 hours at 3 A cm^{-2} for the 100 nm channel SnSe NF device.

SnSe and the anode to be 100 nm and the bias voltage as 0.5 V. The simulation shows that the electric field concentrates around the apex of the NF tip and gradually decreases along the tip's radial direction; on the other hand, the electric field of the SC is uniform for the entire surface. The simulation suggests that the NF emits electrons first from the tip's apex due to the concentrated field; as the voltage increases, the electric field along the radial direction gradually reaches the turn-on field, thus beginning to emit electrons. This is reflected in our data shown in Fig. 3a, in which the emission current is gradually increased with voltage (NF data in Fig. 3a). For the SC, the simulation suggests that once the turn-on voltage is reached for the flat surface, the entire surface would emit at once. From the simulation, we can clearly see that the NF is a better emitter than the SC purely due to the morphology of the NF that concentrates the electrostatic field; however, the NF emits electrons only from its tip, while the SC emits electrons from its whole flat surface. Thus, the NF has a higher field enhancement factor than the SC.

We further study the channel length dependence of SnSe NF field emission and determine the distance dependence of the turn-on voltage and field enhancement factor. Fig. 4a shows the distance dependence of field emission and Fig. 4b shows the FN plot of the SnSe NF. The extracted field enhancement factor at the second emission region of the NF tip for 100 nm, 250 nm, 600 nm, 3 μm, and 6 μm channels are 7930, 5730, 3010, 6190 and 13 800, respectively, and the extracted turn-on voltages are 0.40 V, 1.15 V, 2.32 V, 4.44 V, and 9.87 V, respectively. Fig. 4a and b show that as the channel length increases, the turn-on voltage increases due to more voltage required to maintain the same electric field.

We also noticed that the non-monochronic channel length dependence of the field enhancement factor is observed in our measurement (Fig. 4c). The decreases and then increases of the field enhancement factor with the channel length cannot be simply described using the increasing field enhancement factor at large channel lengths;[64–69] however, such a behavior has been observed in the literature for field emission devices with extremely small channels.[70–74] The increases of the field enhancement factor at small channel lengths is due to the local electric field at the tip's apex reaching infinity as the channel length approaches zero, while the macroscopic electric field far away from the tip reaches a finite value. To qualitatively understand this trend, we consider the empirical field enhancement factor for large channel lengths greater than a few micrometers as[65,68]

$$\beta = Ch + C_0 \tag{4}$$

where h is the channel length and C and C_0 are fitting constants. With small channel lengths less than one micrometer, Edgcombe and Valdre modelled the field enhancement factor as[73,75]

$$\beta = \beta_0\left\{1 + A\left(\frac{h+l}{h}\right) - B\left(\frac{h}{h+l}\right)\right\} \tag{5}$$

where β_0 is the geometry dependence field enhancement factor, l is the height of the emitter, and A and B are fitting constants. As mentioned, eqn (4) and (5) are inconsistent with one another; to make the equations consistent, we combine the two equations as

$$\beta = \left\{C_1 + C_2\left(\frac{h+l}{h}\right) - C_3\left(\frac{h}{h+l}\right)\right\} + C_4 h \tag{6}$$

In eqn (6), we use the fitting constant C_1 instead of β_0 because there is no theoretical work that we are aware of to predict the field enhancement factor of the NF. We use 1.2 μm as our l, and 4894, 291, 12 383, and 3164 as our C_1, C_2, C_3, and C_4, respectively, to fit eqn (6) fairly well with our data (Fig. 4c). As shown in Fig. 4c, at large channel lengths, the linear term dominates and the field enhancement factor varies linearly with the channel length (black line in Fig. 4c), and at small channel lengths, the non-linear term dominates (blue curve in Fig. 4c). The transition point appears when the channel length is comparable with the emitter's length. Physically, as the channel length decreases from the large channel length, the enhancement factor linearly decreases because the emission geometry approaches plane to plane geometry. However, at the transition point, the local electric field around the tip increases faster than the macroscopic electric field far away from the tip; thus, the field enhancement factor increases. Therefore, in this region, the field enhancement factor is the combination of the decreases of the field enhancement factor due to the plane to plane transition and the increase of the field enhancement factor due to the rapid increase of the local electric field.

Interestingly, field emission still happens in air with a 6 μm channel; we try to measure field emission stability with large channel lengths, but the current quickly decays. This result is well expected since the channel length is above the mean free path of electrons in air (~200 nm).[31] We do not think that the reason for the current decay is air ionization since our operating voltage is much smaller than the required breakdown voltages.[76–78] Thus, the current decay is most likely from electron scattering with air molecules. We also measure emission stability using the 100 nm channel length and observe a more stable emission current (Fig. 4d). The emission is stable at 3 A cm^{-2} for 20 hours with less than ±5% fluctuations; in comparison, carbon nanotubes, MoS_2, and graphene emitters usually have fluctuations on the order of ±10% for three hours under high vacuum.[49,79,80] We attribute the higher stability of SnSe to the small channel length and the high bond energy of SnSe. Finally, we compare the performance of the SnSe NF with other materials[34,38,40,50,61,65,68,81,82] and notice that the SnSe NF devices require a lower turn-on voltage (Fig. 5a). The reduced turn-on voltage for field emission is due to its intrinsic low work function and high surface-enhanced electrostatic field (Fig. 5b), thus providing an advantage for small power operation.

In summary, we demonstrate high-performance and stable field emission of single SnSe nanostructures in air. With the device channel down to 100 nm, we studied field emission

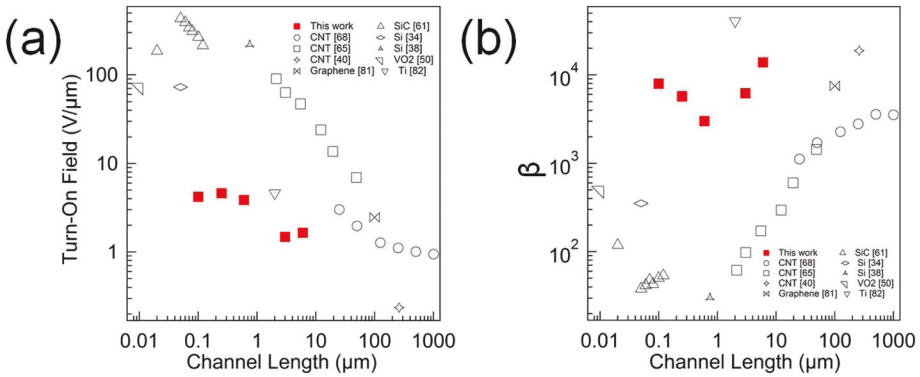

Fig. 5 Performance comparison between this work and the reported literature studies. (a) The turn-on fields and (b) the field enhancement factors of SnSe devices are plotted with channel length dependence, in comparison with the data from literature studies.

from different surface morphologies and observed a significant performance improvement of nanoflower surfaces due to the high aspect ratio. Moreover, the SnSe NF requires only 0.5 V bias voltage to facilitate field emission, which is lower compared to most reported studies; such a low turn-on voltage is desirable for low power applications. We further investigate the emission of the SnSe NF with different channel lengths and conclude that the dependence of the field enhancement factor on the non-monochronic channel length is due to the rapid increase of the local electric field at the tip of the SnSe NF as the channel length decreases. Our results show that SnSe nanostructures are a promising material for vacuum field emission and show promise for rational materials design at the nanoscale to develop new building blocks beyond conventional electronics in the post-Moore's law era.

Conflicts of interest

There are no conflicts to declare.

Acknowledgements

Y. H. acknowledges support from a CAREER award through the National Science Foundation, a Young Investigator Award through the United States Air Force Office of Scientific Research, a PRF Doctoral New Investigator Award from the American Chemical Society, the UCLA Sustainable LA Grand Challenge, and the Anthony and Jeanne Pritzker Family Foundation.

References

1 M. Waldrop, *Nature*, 2016, **530**, 144–147.
2 International Technology Roadmap for Semiconductors, *ITRS 2.0 2015 Ed.*, http://www.itrs2.net/.
3 J. S. Kang, M. Li, H. Wu, H. Nguyen and Y. Hu, *Science*, 2018, **361**, 575–578.
4 T. N. Theis and P. M. Solomon, *Science*, 2010, **327**, 1600–1601.
5 A. D. Franklin, *Science*, 2015, **349**, aab2750.
6 W. Lu and C. M. Lieber, *Nat. Mater.*, 2007, **6**, 841–850.
7 R. Chau, B. Doyle, S. Datta, J. Kavalieros and K. Zhang, *Nat. Mater.*, 2007, **6**, 810–812.
8 M. Lundstrom, *Science*, 2003, **299**, 210–211.
9 M. Luisier, M. Lundstrom, D. A. Antoniadis and J. Bokor, *IEEE Int. Electron Devices Meet.*, 2011, 11.2.1–11.2.4.
10 J. S. Kang, H. Wu and Y. Hu, *Nano Lett.*, 2017, **17**, 7507–7514.
11 Y. Hu, J. Xiang, G. Liang, H. Yan and C. M. Lieber, *Nano Lett.*, 2008, **8**, 925–930.
12 J. Xiang, W. Lu, Y. Hu, Y. Wu, H. Yan and C. M. Lieber, *Nature*, 2006, **441**, 489–493.
13 Y. Hu, H. O. H. Churchill, D. J. Reilly, J. Xiang, C. M. Lieber and C. M. Marcus, *Nat. Nanotechnol.*, 2007, **2**, 622–625.
14 Y. Hu, F. Kuemmeth, C. M. Lieber and C. M. Marcus, *Nat. Nanotechnol.*, 2012, **7**, 47–50.
15 H. Yan, H. S. Choe, S. Nam, Y. Hu, S. Das, J. F. Klemic and J. C. Ellenbogen, *Nature*, 2011, **470**, 240–244.
16 Q. Cao, J. Tersoff, D. B. Farmer, Y. Zhu and S. Han, *Science*, 2017, **356**, 1369–1372.
17 C. Qiu, Z. Zhang, M. Xiao, Y. Yang, D. Zhong and L. Peng, *Science*, 2017, **355**, 271–276.
18 Z. Zhong, N. M. Gabor, J. E. Sharping, A. L. Gaeta and P. L. Mceuen, *Nat. Nanotechnol.*, 2008, **3**, 201–205.
19 A. Javey, J. Guo, Q. Wang, M. Lundstrom and H. Dai, *Nature*, 2003, **424**, 654–657.
20 L. Liao, Y. Lin, M. Bao, R. Cheng, J. Bai, Y. Liu, Y. Qu, K. L. Wang, Y. Huan and X. Duan, *Nature*, 2010, **467**, 305–308.
21 K. S. Novoselov, A. K. Geim, S. V. Morozov, D. Jiang, Y. Zhang, S. V. Dubonos, I. V. Grigorieva and A. A. Firsov, *Science*, 2004, **306**, 666–669.
22 D. Hisamoto, W. Lee, J. Kedzierski, H. Takeuchi, K. Asano, C. Kuo, E. Anderson, T. King, J. Bokor and C. Hu, *IEEE Trans. Electron Devices*, 2000, **47**, 2320–2325.
23 H. S. P. Wong, *IBM J. Res. Dev.*, 2002, **46**, 133–168.

24 H. Tsai, J. W. Pitera, H. Miyazoe, S. Bangsaruntip, S. U. Engelmann, C. Liu, J. Y. Cheng, J. J. Bucchignano, D. P. Klaus, E. A. Joseph, D. P. Sanders, M. E. Colburn and M. A. Guillorn, *ACS Nano*, 2014, **8**, 5227–5232.
25 D. Sarkar, X. Xie, W. Liu, W. Cao, J. Kang, Y. Gong, S. Kraemer, P. M. Ajayan and K. Banerjee, *Nature*, 2015, **526**, 91–95.
26 D. M. Newns, B. G. Elmegreen, X. Liu and G. J. Martyna, *Adv. Mater.*, 2012, **24**, 3672–3677.
27 S. Salahuddin and S. Datta, *Nano Lett.*, 2008, **8**, 405–410.
28 D. A. Allwood, G. Xiong, C. C. Faulkner, D. Atkinson, D. Petit and R. P. Cowburn, *Science*, 2005, **309**, 1688–1693.
29 J. J. Yang, D. B. Strukov and D. R. Stewart, *Nat. Nanotechnol.*, 2013, **8**, 13–24.
30 S. H. Jo, T. Chang, I. Ebong, B. B. Bhadviya, P. Mazumder and W. Lu, *Nano Lett.*, 2010, **10**, 1297–1301.
31 J. Han and M. Meyyappan, *IEEE Spectrum*, 2014, **51**, 31–35.
32 B. R. Stoner and J. T. Glass, *Nat. Nanotechnol.*, 2012, **7**, 485–487.
33 T. Utsumi, *IEEE Trans. Electron Devices*, 1991, **38**, 2276–2283.
34 J. Han, D. Moon and M. Meyyappan, *Nano Lett.*, 2017, **17**, 2146–2151.
35 J. Han, J. S. Oh and M. Meyyappan, *IEEE Trans. Nanotechnol.*, 2014, **13**, 464–468.
36 S. Srisonphan, Y. S. Jung and H. K. Kim, *Nat. Nanotechnol.*, 2012, **7**, 504–508.
37 B. L. Pescini, A. Tilke, R. H. Blick, H. Lorenz, J. P. Kotthaus, W. Eberhardt and D. Kem, *Adv. Mater.*, 2001, **13**, 1780–1783.
38 C. A. Spindt, C. E. Holland, A. Rosengreen and I. Brodie, *IEEE Trans. Electron Devices*, 1991, **38**, 2355–2363.
39 P. Hou, C. Liu and H. Cheng, in *Nanomaterials Handbook*, 2nd edn, 2017, pp. 255–272.
40 S. H. Jo, D. Z. Wang, J. Y. Huang, W. Z. Li, K. Kempa and Z. F. Ren, *Appl. Phys. Lett.*, 2004, **85**, 4.
41 S. Kumar, G. S. Duesberg, R. Pratap and S. Raghavan, *Appl. Phys. Lett.*, 2014, **105**, 5.
42 D. Ye, S. Moussa, J. D. Ferguson, A. A. Baski and M. S. El-shall, *Nano Lett.*, 2012, **12**, 1265–1268.
43 Z. Wu, S. Pei, W. Ren, D. Tang, L. Gao, B. Liu, F. Li, C. Liu and H. Cheng, *Adv. Mater.*, 2009, **21**, 1756–1760.
44 D. J. Late, P. A. Shaikh, R. Khare, R. V. Kashid, M. Chaudhary, M. A. More and S. B. Ogale, *ACS Appl. Mater. Interfaces*, 2014, **6**, 15881–15888.
45 M. B. Erande, S. R. Suryawanshi, M. A. More and D. J. Late, *Eur. J. Inorg. Chem.*, 2015, **19**, 3102–3107.
46 A. L. Koh, E. Gidcumb, O. Zhou and R. Sinclair, *Nanoscale*, 2016, **8**, 16405–16415.
47 W. B. Choi, D. S. Chung, J. H. Kang, H. Y. Kim, Y. W. Jin, I. T. Han, Y. H. Lee, J. E. Jung, N. S. Lee, G. S. Park and J. M. Kim, *Appl. Phys. Lett.*, 1999, **75**, 3129–3131.
48 B. D. Banerjee, S. H. Jo and Z. F. Ren, *Adv. Mater.*, 2004, **16**, 2028–2032.
49 B. Z. Pan, H. Lai, F. C. K. Au, X. Duan, W. Zhou, W. Shi, N. Wang, C. Lee, N. Wong, S. Lee and S. Xie, *Adv. Mater.*, 2000, **12**, 1186–1190.
50 M. Liu, W. Fu, Y. Yang, T. Li and Y. Wang, *Appl. Phys. Lett.*, 2018, **112**, 5.
51 C. Li, M. T. Cole, W. Lei, K. Qu, K. Ying, Y. Zhang, A. R. Robertson, J. H. Warner, S. Ding, X. Zhang, B. Wang and W. I. Milne, *Adv. Funct. Mater.*, 2014, **24**, 1218–1227.
52 C. S. Rout, P. D. Joshi, R. V. Kashid, D. S. Joag, M. A. More, A. J. Simbeck, M. Washington, S. K. Nayak and D. J. Late, *Sci. Rep.*, 2013, **3**, 8.
53 Y. B. Li, Y. Bando and D. Golberg, *Appl. Phys. Lett.*, 2003, **82**, 1962–1964.
54 *Handbook of Chemistry and Physics*, ed. D. R. Lide, CRC Press, 87th edn, 2006.
55 X. Fan, W. T. Zheng, J. Kuo and D. J. Singh, *J. Phys.: Condens. Matter*, 2015, **27**, 5.
56 Z. Cui, X. Wang, Y. Ding and M. Li, *Superlattices Microstruct.*, 2018, **114**, 251–258.
57 H. Ju and J. Kim, *ACS Nano*, 2016, **10**, 5730–5739.
58 L.-D. Zhao, S.-H. Lo, Y. Zhang, H. Sun, G. Tan, C. Uher, C. Wolverton, V. P. Dravid and M. G. Kanatzidis, *Nature*, 2014, **508**, 373–377.
59 I. Loa, R. J. Husband, R. A. Downie, S. R. Popuri and J. G. Bos, *J. Phys.: Condens. Matter*, 2015, **27**, 7.
60 L. Li, Z. Chen, Y. Hu, X. Wang, T. Zhang, W. Chen and Q. Wang, *J. Am. Chem. Soc.*, 2013, **135**, 1213–1216.
61 M. Liu, T. Li and Y. Wang, *J. Vac. Sci. Technol., B: Nanotechnol. Microelectron.: Mater., Process., Meas., Phenom.*, 2017, **35**, 5.
62 I. Brodie, *J. Appl. Phys.*, 1964, **35**, 2324–2332.
63 R. G. Forbes, *Proc. R. Soc. London, Ser. A*, 2013, **469**, 16.
64 T. Cheng, P. Chen and S. Wu, *Nanoscale Res. Lett.*, 2012, **7**, 6.
65 Z. Xu, X. D. Bai and E. G. Wang, *Appl. Phys. Lett.*, 2006, **23**, 3.
66 R. C. Smith, J. D. Carey, R. D. Forrest and S. R. P. Silva, *J. Vac. Sci. Technol., B: Microelectron. Nanometer Struct.–Process., Meas., Phenom.*, 2005, **23**, 632–635.
67 R. C. Smith, D. C. Cox and S. R. P. Silva, *Appl. Phys. Lett.*, 2005, **87**, 3.
68 J. Bonard, M. Croci, I. Arfaoui, O. Noury, D. Sarangi and A. Chatelain, *Diamond Relat. Mater.*, 2002, **11**, 763–768.
69 L. Nilsson, O. Groening, C. Emmenegger, O. Kuettel, E. Schaller, L. Schlapbach, H. Kind, J. Bonard and K. Kern, *Appl. Phys. Lett.*, 2000, **76**, 2071–2073.
70 P. Zhang, S. B. Fairchild, T. C. Back and Y. Luo, *AIP Adv.*, 2017, **7**, 6.
71 J. Lin, P. Y. Wong, P. Yang, Y. Y. Lau, W. Tang and P. Zhang, *J. Appl. Phys.*, 2017, **121**, 6.
72 J. Bonard, K. A. Dean, B. F. Coll and C. Klinke, *Phys. Rev. Lett.*, 2002, **19**, 4.
73 C. J. Edgcombe and U. Valdre, *J. Microsc.*, 2001, **203**, 188–194.

74 F. M. Charbonnier, W. A. Mackie, R. L. Hartman and T. Xie, *J. Vac. Sci. Technol., B: Microelectron. Nanometer Struct.–Process., Meas., Phenom.*, 2001, **19**, 1064–1072.
75 C. J. Edgcombe and U. Valdre, *Philos. Mag.*, 2002, **82**, 987–1007.
76 A. Peschot, N. Bonifaci, O. Lesaint, C. Valadares and C. Poulain, *Appl. Phys. Lett.*, 2014, **105**, 4.
77 Y. Hirata, K. Ozaki, U. Ikeda and M. Mizoshiri, *Thin Solid Films*, 2007, **515**, 4247–4250.
78 E. Hourdakis, G. W. Bryant and N. M. Zimmerman, *J. Appl. Phys.*, 2006, **100**, 6.
79 R. V. Kashid, D. J. Late, S. S. Chou, Y. Huang, M. De, D. S. Joag, M. A. More and V. P. Dravid, *Small*, 2013, **9**, 2730–2734.
80 W. Heer, A. Chatelain and U. Ugarte, *Science*, 1995, **270**, 1179–1180.
81 A. Malesevic, R. Kemps, A. Vanhulsel, M. P. Chowdhury, A. Volodin and C. Van Haesendonck, *J. Appl. Phys.*, 2008, **104**, 6.
82 S. Pennisi, G. Castorina and D. Patti, *IEEE Trans. Electron Devices*, 2015, **62**, 4293–4300.